coatings

MDPI

Article

Characterization and Photovoltaic Properties of $BiFeO_3$ Thin Films

Yasuhiro Shirahata and Takeo Oku *

Department of Materials Science, The University of Shiga Prefecture, 2500 Hassaka, Hikone, Shiga 522-8533, Japan; shirahata.y@mat.usp.ac.jp

* Correspondence: oku@mat.usp.ac.jp; Tel.: +81-749-28-8368

Academic Editor: Francesco Di Benedetto

Received: 19 August 2016; Accepted: 5 December 2016; Published: 8 December 2016

Abstract: Bismuth ferrite ($BiFeO_3$) thin films were prepared by a spin-coating method. Crystal structure and optical properties of the $BiFeO_3$ films were evaluated using X-ray diffraction. The lattice constants, crystallite size, and energy gap of $BiFeO_3$ films depended on the concentration of the $BiFeO_3$ precursor solution. $BiFeO_3/CH_3NH_3PbI_3$ photovoltaic devices were fabricated to investigate photovoltaic properties of $BiFeO_3$. Current density–voltage characteristics of the photovoltaic devices showed rectifying behavior, indicating that $BiFeO_3$ worked as an electron transport layer in $CH_3NH_3PbI_3$-based photovoltaic devices.

Keywords: bismuth ferrite; thin films; photovoltaic property; $CH_3NH_3PbI_3$

1. Introduction

Bismuth ferrite ($BiFeO_3$) has attracted much attention among researchers, because $BiFeO_3$ is used for potential applications, such as information storage, spintronics, and ferroelectric devices [1–5]. In addition, photovoltaic properties of $BiFeO_3$ bulks, $BiFeO_3$/semiconductor, and $BiFeO_3$/ferroelectric heterostructures have been extensively investigated [6–11]. However, photovoltaic properties are sensitive to fabrication process, electronic structure, and interfacial condition. Therefore, precise characterization of $BiFeO_3$ and investigation of $BiFeO_3$-based solar cells are of importance.

Very recently, $BiFeO_3$ films prepared by spin-coating method were used for $CH_3NH_3PbI_3$-based photovoltaic devices [9]. $CH_3NH_3PbI_3$ with perovskite structure is known as a fascinating light absorber, and the $CH_3NH_3PbI_3$-based solar cell is anticipated as a next-generation solar cell [12–19]. $BiFeO_3$ films act as electron transport layers because $BiFeO_3$ is an *n*-type semiconductor. However, optical and photovoltaic properties of the $BiFeO_3/CH_3NH_3PbI_3$ photovoltaic devices are still unknown.

The purpose of the present work is to characterize $BiFeO_3$ thin films prepared by a simple spin-coating method and investigate photovoltaic properties of $BiFeO_3/CH_3NH_3PbI_3$ photovoltaic devices. The crystal structures of the $BiFeO_3$ thin films prepared from precursor solutions with different concentrations were characterized by X-ray diffraction (XRD). The optical properties of the $BiFeO_3$ films were investigated by collecting optical absorption spectra. The photovoltaic properties of the $BiFeO_3/CH_3NH_3PbI_3$ devices were investigated by measuring current density–voltage (*J*–*V*) characteristics and incident photon to current conversion efficiency (IPCE).

2. Materials and Methods

$BiFeO_3$ thin films were prepared on glass substrates by spin-coating method in air atmosphere [20]. Solutions of $BiFeO_3$ with different concentrations were prepared from bismuth nitrate penehydrate ($Bi(NO_3)_3{\cdot}5H_2O$) (99.5%, Wako Pure Chemical Industries, Ltd., Osaka, Japan), iron(III) nitrate nonahydrate ($Fe(NO_3)_3{\cdot}9H_2O$) (99.0%, Wako Pure Chemical Industries, Ltd.), citric acid

(99.5%, Yoneyama Yakuhin Kogyo Co., Ltd., Osaka, Japan), and 2-methoxyethanol (99.0%, 2 mL, Wako Pure Chemical Industries, Ltd.). Citric acid was used as a chelating agent. The concentration of the precursor solution was varied from 0.05 to 0.30 M. Excess 10% $Bi(NO_3)_3 \cdot 5H_2O$ was added to compensate for Bi loss during annealing. The $BiFeO_3$ solution was dropped on the glass substrate, and was spun at 3000 rpm for 30 s by a spin coater (MS-A100, Mikasa Co., Ltd., Tokyo, Japan). Then, the $BiFeO_3$ precursor film was dried on a hotplate (ND-1, As One Corporation, Osaka, Japan) at 150 °C for 5 min. This process was repeated five times. Finally, the precursor film was annealed in an electric furnace (SMF-1, As One Corporation) at 500 °C for 1 h. Photovoltaic devices with $BiFeO_3/CH_3NH_3PbI_3$ structure were also fabricated by the spin-coating method. Concerning energy level of $BiFeO_3/CH_3NH_3PbI_3$ structure, $BiFeO_3$ and $CH_3NH_3PbI_3$ are a good combination, because $BiFeO_3$ is an *n*-type semiconductor [16,21,22]. The fabrication process of the $BiFeO_3/CH_3NH_3PbI_3$ photovoltaic devices is as follows [23]. First, 0.05 M $BiFeO_3$ precursor layer was spin-coated onto a fluorine-doped tin oxide (FTO)-coated glass substrate by the spin-coater at 3000 rpm for 30 s, and was dried onto the hot plate at 150 °C for 5 min. This process was repeated three times. Subsequently, the $BiFeO_3$ layer was annealed in an electric furnace at 500 °C for 30 min. After cooling to room temperature, a 0.10 M $BiFeO_3$ layer was spin-coated onto the 0.05 M $BiFeO_3$ layer at 3000 rpm for 30 s, and was dried onto the hot plate at 150 °C for 5 min. This process was repeated three times. The 0.10 M $BiFeO_3$ layer was annealed in the electric furnace at 500 °C for 2 h. In the present work, a one-step solution deposition method was employed to prepare $CH_3NH_3PbI_3$ layers [23–29]. The preparation process was as follows: a mixed solution consisting of methylammonium iodine (CH_3NH_3I, 98.8 mg, Showa Chemical Co., Ltd., Tokyo, Japan), PbI_2 (289.3 mg, Sigma-Aldrich, St. Louis, MO, USA), and γ-butyrolactone (500 μL, Wako Pure Chemical Industries, Ltd.) was prepared by stirring at 60 °C for 2 h in a water bath (BH-22, Masuda Corporation, Osaka, Japan,) attached with a magnetic stirrer (Heracles-20, Koike Precision Instruments, Hyogo, Japan). The $CH_3NH_3PbI_3$ layer was spin-coated on the $BiFeO_3$ layer at 2000 rpm for 60 s. This process was repeated four times. The spin-coated $CH_3NH_3PbI_3$ layer was annealed at 100 °C for 15 min. After cooling to room temperature, a hole transport layer was spin-coated on the $CH_3NH_3PbI_3$ layer at 4000 rpm for 20 s. As the hole transport material, 2,2′,7,7′-tetrakis-(*N*,*N*-di-p-methoxyphenylamine)-9,9′-spirobifluorene (spiro-OMeTAD) was used because spiro-OMeTAD can yield higher conversion efficiencies due to its amorphous structure and reasonable hole mobility [30]. The spiro-OMeTAD powder (36.1 mg, Luminescence Technology, Hsinchu City, Taiwan) was dissolved in chlorobenzene (Wako Pure Chemical Industries, Ltd., 500 μL). Solutions of lithium bis(trifluomethylsulfonyl) imide (Li-TFSI, 8.8 μL)and 4-*tert*-butylpyridine (14.4 μL, Sigma-Aldrich) were added into the spiro-OMeTAD solution. The Li-TFSI solution was prepared by dissolving Li-TFSI powder (260 mg, Tokyo Chemical Industry Co., Ltd., Tokyo, Japan) in acetonitrile (0.5 mL, Wako Pure Chemical Industries, Ltd.). Finally, gold (Au) counter electrodes were thermally deposited on the hole transport layer. For comparison, a photovoltaic device without $BiFeO_3$ layer was fabricated.

The crystal structure of the $BiFeO_3$ thin films was characterized by an X-ray diffractometer (D2 PHASER, Bruker Corporation, Billerica, MA, USA) with CuKα radiation. The film thickness of the $BiFeO_3$ films was checked by atomic force microscopy (AFM) (SPI-3800N/SPA-400, SII Nanotechnology Inc., Chiba, Japan). The optical absorption spectra of the $BiFeO_3$ and $CH_3NH_3PbI_3$ films were collected using ultraviolet–visible–near-infrared spectrophotometer (V-770, Jasco Corporation, Tokyo, Japan). The *J*–*V* characteristics of the photovoltaic devices were recorded using a potentiostat (HSV-110, Hokuto Denko Corporation, Hyogo, Japan). The devices were irradiated under simulated AM 1.5 ($100\ mW \cdot cm^{-2}$) conditions through the bottom of FTO-coated glass substrate by solar simulator (XES-301S, San-Ei Electric Co., Ltd., Osaka, Japan). The effective area of the devices was $0.090\ cm^2$. IPCE spectra of the devices were collected using an IPCE measurement system (QE-R, Enli Technology Co., Ltd., Kaohsiung City, Taiwan). All measurements were performed at room temperature.

3. Results and Discussion

Figure 1a shows XRD patterns of the $BiFeO_3$ thin films. It was confirmed that the $BiFeO_3$ films were polycrystalline with a rhombohedral system. $BiFeO_3$ is usually classed as rhombohedral space group R3*c* structure with lattice parameter of a_{rh} = 0.5634 nm and interaxial angle of α_{rh} = 59.348° [31]. To later discuss lattice distortion in the present $BiFeO_3$ films, the XRD patterns of the $BiFeO_3$ films were indexed on the basis of hexagonal unit cell of $BiFeO_3$, as shown in Figure 1b. Moreover, the film thicknesses of the 0.10 M, 0.20 M, and 0.30 M $BiFeO_3$ films were 224, 336, and 367 nm, respectively; i.e., the film thickness of $BiFeO_3$ films was proportional to the concentration of $BiFeO_3$ precursor solution. This behavior was almost the same as a previous report [32]. The lattice constants of the $BiFeO_3$ were estimated from Equation (1):

$$\frac{1}{d^2} = \frac{4}{3}\frac{h^2 + hk + k^2}{a^2} + \frac{l^2}{c^2} \tag{1}$$

Here, *a*, *c*, *d*, and (*hkl*) are the lattice constants of *a*- and *c*-axes, interplanar lattice spacing, and Miller indices, respectively. As shown in Figure 1c, the estimated lattice constants were compatible with those of $BiFeO_3$ bulk [31,33]. On the other hand, the lattice constant of the *a*-axis slightly increased with increasing concentration of $BiFeO_3$ precursor solution, while that of the *c*-axis significantly increased at a concentration of 0.20 M. The results suggest that stress in the $BiFeO_3$ films relieved at concentration of 0.20 M. Crystallite sizes (*D*) of the $BiFeO_3$ were also estimated from the XRD patterns using Scherrer's equation:

$$D = 0.9\lambda/\beta\cos\theta \tag{2}$$

Here, λ, β, and θ are the X-ray wavelength of 0.154184 nm, full width at half maximum of the diffraction peak, and Bragg angle of the diffraction peak, respectively. In the present study, the averaged *D* values were estimated from *D* values of 012, 104, and 110 diffraction peaks of the $BiFeO_3$. Figure 1d shows the averaged *D* of the $BiFeO_3$. The *D* increased from 42 to 55 nm with increasing concentration of $BiFeO_3$ precursor solution.

Figure 2a shows optical absorption spectra of the $BiFeO_3$ thin films. The absorption cut-off wavelengths of the films were approximately 565 nm, in agreement with a previous report [34–36]. The absorption spectrum of the 0.10 M $BiFeO_3$ film showed a large absorbance in the wavelength from 300 to 450 nm, which is likely associated with lattice distortion in the film. Energy gaps of the $BiFeO_3$ films were calculated by Tauc formula:

$$(\mathrm{h}\nu\alpha)^n = A(h\nu - E_g) \tag{3}$$

Here, h, ν, α, *A*, E_g, and *n* are the Plank constant, light frequency, absorption coefficient, proportional constant, energy gap, and power index which depends on the nature of the transition, respectively. In the present study $n = 2$ was used for the $BiFeO_3$ because $BiFeO_3$ is a direct transition semiconductor [36,37]. The E_g were estimated by extrapolating the linear part of the Tauc plots to meet $(\mathrm{h}\nu\alpha)^2 = 0$, as shown in shown in Figure 2c. The estimated E_g values corresponded to previous reports [6,9,36,37]. On the other hand, the estimated E_g decreased with increasing concentration of $BiFeO_3$ precursor solution, indicating that E_g depended on the concentration of the $BiFeO_3$ solution. Furthermore, the largest E_g was obtained for the 0.10 M $BiFeO_3$ film, which would be a result of lattice distortion in the films.

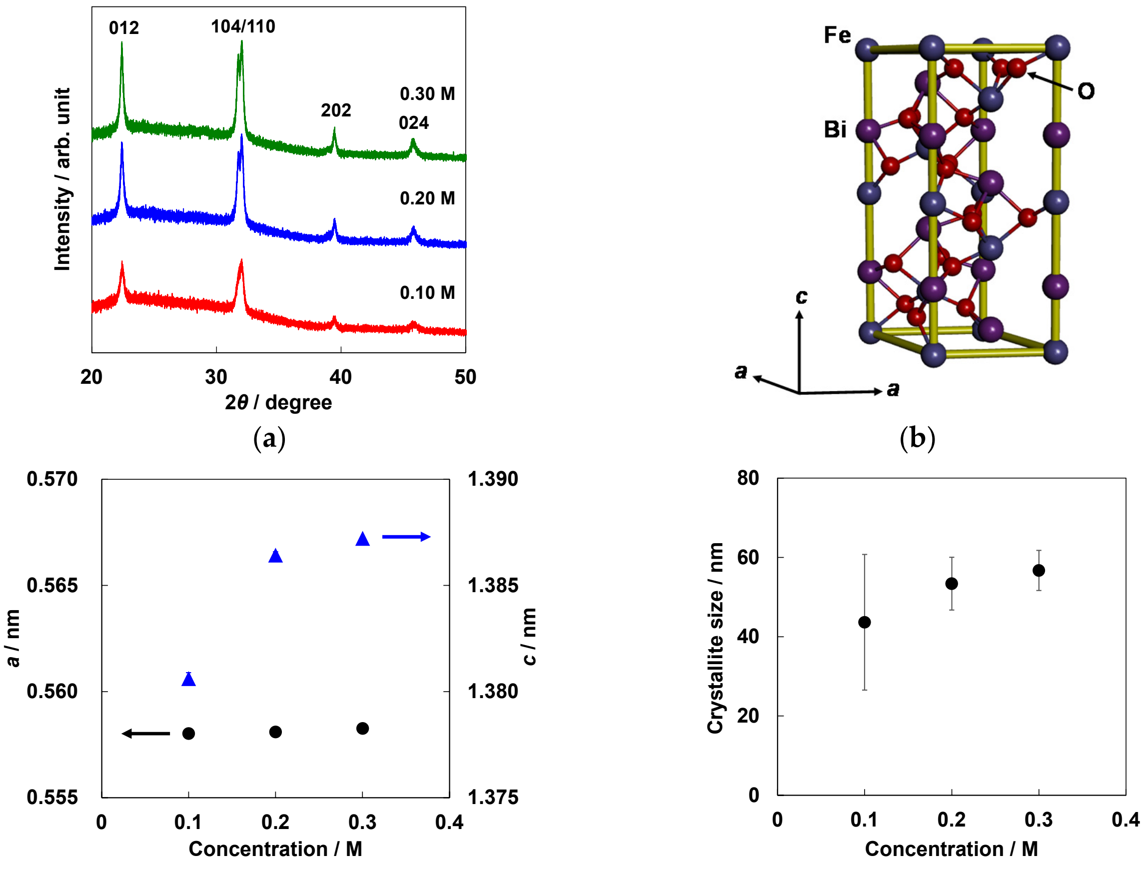

(**a**) (**b**)

(**c**) (**d**)

Figure 1. (**a**) X-ray diffraction (XRD) patterns of $BiFeO_3$ thin films grown on glass substrates; (**b**) Schematic illustration of hexagonal unit cell of $BiFeO_3$; (**c**) Lattice constants and (**d**) crystallite sizes of $BiFeO_3$ as a function of concentration of $BiFeO_3$ precursor solution. The crystallographic information data of (**b**) was downloaded from Ref. [38].

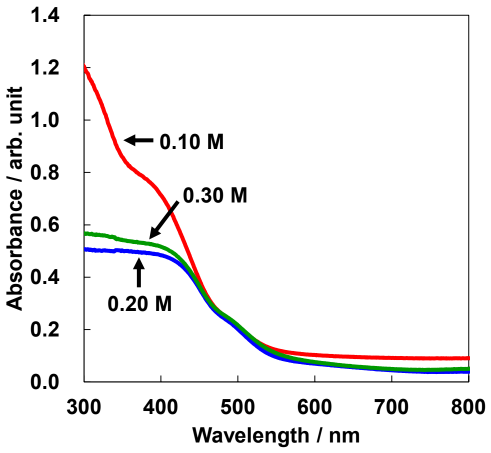

(**a**)

Figure 2. *Cont.*

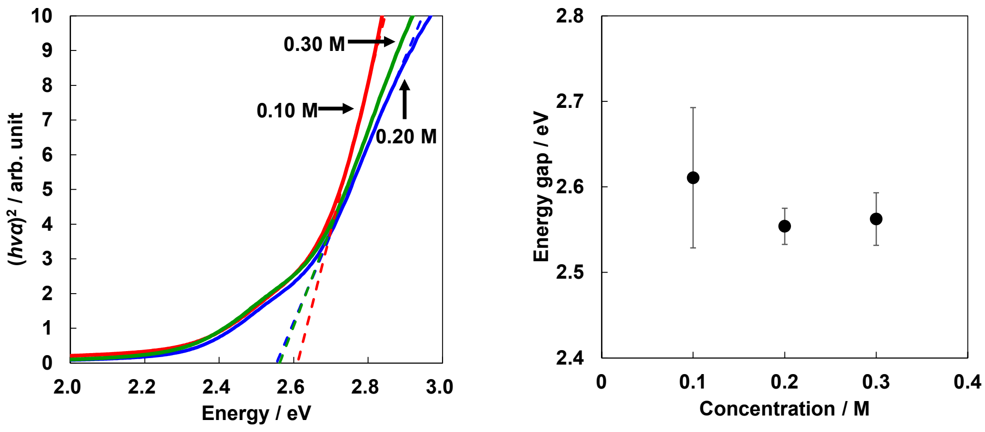

(**b**) (**c**)

Figure 2. (**a**) Optical absorption spectra of $BiFeO_3$ thin films grown on glass substrates; (**b**) Tauc plots of $BiFeO_3$ films; (**c**) Energy gaps of $BiFeO_3$ films as a function of concentration of the $BiFeO_3$ precursor solution.

To discuss the lattice distortion in the $BiFeO_3$ films, a simple calculation was attempted using Hooke's law:

$$\Delta\varepsilon = \sigma/E \tag{4}$$

where $\Delta\varepsilon$, σ, E are the strain, stress, and Young's modulus, respectively. In the present study, previously reported Young's modulus of $BiFeO_3$ was used [39]. The lattice strains for *a*- and *c*-axes ($\Delta\varepsilon_a$ and $\Delta\varepsilon_c$) are given as follows:

$$\Delta\varepsilon_a = (a' - a)/a \tag{5}$$

and

$$\Delta\varepsilon_c = (c' - c)/c \tag{6}$$

Here, a' and c' are the lattice constants of $BiFeO_3$ bulk [33]. The calculated σ values for *a*- and *c*-axes of $BiFeO_3$ as a function of film thickness are shown in Figure 3. The σ for *a*-axis slightly increased with increasing film thickness, while that for *c*-axis significantly increased: the stress for *c*-axis strongly depended on film thickness. Furthermore, a sign reversal of the σ for *c*-axis occurred at a film thickness of 367 nm (0.30 M), considering that the 0.10 and 0.20 M $BiFeO_3$ films were wholly under compressive stress, while the 0.30 M $BiFeO_3$ film was partially under tensile stress. Accordingly, a series of variations in crystal structure and optical properties were attributed to compressive stress relaxation in the $BiFeO_3$ films that depended on film thickness.

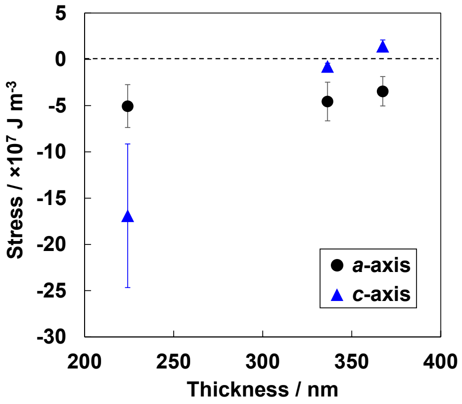

Figure 3. Stresses along *a*- (filled circle) and *c*-axes (filled triangle) of $BiFeO_3$ as a function of film thickness of $BiFeO_3$.

Figure 4a shows *J*–*V* curves of the FTO/$BiFeO_3$/$CH_3NH_3PbI_3$/spiro-OMeTAD/Au and FTO/$CH_3NH_3PbI_3$/spiro-OMeTAD/Au device photovoltaic devices under light irradiation. A clear rectifying behavior was seen for the FTO/$BiFeO_3$/$CH_3NH_3PbI_3$/spiro-OMeTAD/Au device, while a linear *J*–*V* curve was seen for the FTO/$CH_3NH_3PbI_3$/spiro-OMeTAD/Au one, ensuring that the $BiFeO_3$ acted as an electron transport layer in the present device. From these *J*–*V* curves, a short-circuit current density (J_{sc}) of 0.290 mA cm^{-2}, open-circuit voltage (V_{oc}) of 0.531 V, fill factor (FF) of 0.414, and conversion efficiency (η) of 0.064% were obtained for the FTO/$BiFeO_3$/$CH_3NH_3PbI_3$/spiro-OMeTAD/Au device. In contrast, a J_{sc} of 0.652 mA cm^{-2}, V_{oc} of 0.014 V, FF of 0.227, and η of 0.002% were obtained for the FTO/$CH_3NH_3PbI_3$/spiro-OMeTAD/Au one. However, the η was quite small compared to the previous report [9]. As one of the possible reasons for the low conversion efficiency, external factors such as temperature, humidity, and fabrication process were considered [40]. An IPCE spectrum of the FTO/$BiFeO_3$/$CH_3NH_3PbI_3$/spiro-OMeTAD/Au photovoltaic device is shown in Figure 4b. The device showed a broad IPCE spectrum in the wavelength range between 320 and 780 nm, indicating that the generation of free electrons and/or free holes occurred in the $CH_3NH_3PbI_3$ layer under visible light irradiation. An optical absorption spectrum of the same device is also shown in Figure 4b. From the optical absorption spectrum, E_g of the $BiFeO_3$ and $CH_3NH_3PbI_3$ were estimated to be 2.78 and 1.57 eV, respectively.

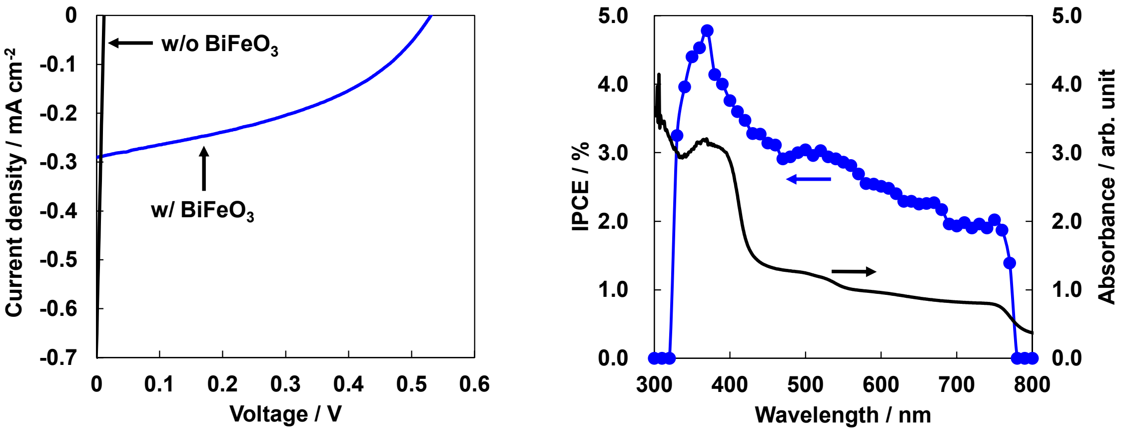

(**a**) (**b**)

Figure 4. (**a**) *J*–*V* curves of FTO/$BiFeO_3$/$CH_3NH_3PbI_3$/spiro-OMeTAD/Au (w/ $BiFeO_3$) and FTO/$CH_3NH_3PbI_3$/spiro-OMeTAD/Au (w/o $BiFeO_3$) devices; (**b**) Incident photon to current conversion efficiency (IPCE) (left) and optical absorption spectra (right) of FTO/$BiFeO_3$/$CH_3NH_3PbI_3$/spiro-OMeTAD/Au device. FTO: fluorine-doped tin oxide; Spiro-OMeTAD: 2,2′,7,7′-tetrakis-(*N*,*N*-di-p-methoxyphenylamine)-9,9′-spirobifluorene.

The photovoltaic mechanism based on energy levels is discussed. Figure 5 shows an energy level diagram of the FTO/$BiFeO_3$/$CH_3NH_3PbI_3$/spiro-OMeTAD/Au photovoltaic device, where previously reported and estimated values were used for the energy levels [16,21,22]. The electronic charge generation occurs in the $CH_3NH_3PbI_3$ layer by light irradiation from the FTO bottom side. Then, the electrons from the $CH_3NH_3PbI_3$ are transferred to the FTO electrode through the $BiFeO_3$ electron transport layer. Similarly, the holes are transferred to Au electrode through the spiro-OMeTAD hole transport layer. It has been known that V_{oc} of inorganic/organic solar cells is related to the energy gaps between the conduction band of the inorganic semiconductor and the valence band of the organic semiconductor. According to the energy level diagram in Figure 5, the theoretical V_{oc} of the $BiFeO_3$/$CH_3NH_3PbI_3$ photovoltaic device can be calculated by the following equation [41]:

$$V_{oc} = \frac{1}{e}(E_c - E_H) - V_{loss} \quad (7)$$

Here, e, E_c, E_H, and V_{loss} are the elementary charge, conduction band of inorganic semiconductor, the highest occupied molecular orbital (HOMO) of the organic semiconductor, and the empirical voltage loss for exciton dislocation at a heterojunction, respectively. Usually, the V_{loss} is 0.3–0.5 V [8,41]. In the present study, the theoretical V_{oc} of the $BiFeO_3/CH_3NH_3PbI_3$ photovoltaic cell was 0.9–1.1 V. These values are greater than the present V_{oc}, as shown in Figure 4a. The obtained low V_{oc} was considered to be due to large V_{loss} associated with trap states in the $CH_3NH_3PbI_3$ layer, presumably generated due to partial separation of PbI_2 from the $CH_3NH_3PbI_3$ [23,24,26–28]. In addition, it is considered that grains of the present $CH_3NH_3PbI_3$ were small. In fact, a correlation between grain size and V_{oc} of $CH_3NH_3PbI_3$-based solar cells was recently reported by Kim et al., and they argued that trap states in $CH_3NH_3PbI_3$ layer decreased accompanied by enlargement of grains [42]. In our opinion, fabricating a completely pinhole-free $CH_3NH_3PbI_3$ film is significantly important to achieve high conversion efficiencies. In addition, to avoid deterioration of photovoltaic devices due to many external factors, further development of solar cells that are durable for external factors is required for the improvement of photovoltaic performance.

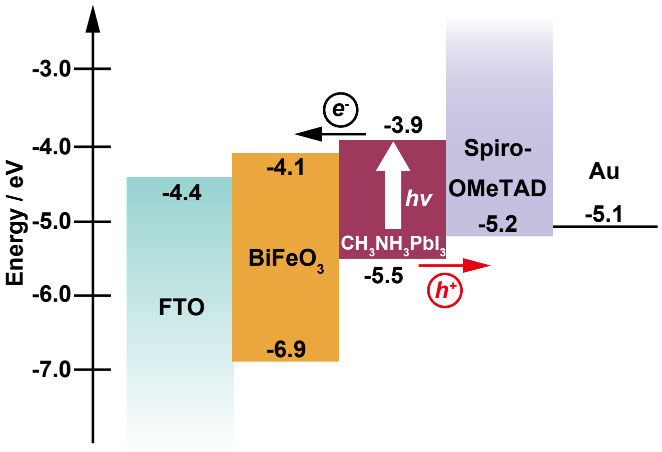

Figure 5. Energy level diagram of FTO/$BiFeO_3/CH_3NH_3PbI_3$/spiro-OMeTAD/Au photovoltaic device.

4. Conclusions

Crystal structures and optical properties of $BiFeO_3$ thin films prepared from precursor solutions with different concentrations were investigated. Polycrystalline $BiFeO_3$ films with a hexagonal system were obtained. The lattice constants, crystallite size, and energy gap of the $BiFeO_3$ films depended on concentration of $BiFeO_3$ precursor solution. The variations in structural parameters and optical properties were attributed to compressive stress relaxation in the $BiFeO_3$ films that depended on film thickness. $BiFeO_3/CH_3NH_3PbI_3$ photovoltaic devices were also fabricated to investigate their photovoltaic properties. The $BiFeO_3/CH_3NH_3PbI_3$ photovoltaic devices showed a rectifying behavior, and a small conversion efficiency was obtained for the present $BiFeO_3/CH_3NH_3PbI_3$ device. From these combined results, $BiFeO_3$ is anticipated as an electron transport layer in solar cells.

Acknowledgments: This work was partly supported by Super Cluster Program of Japan Science and Technology Agency, and Grant-in-Aid for Scientific Research (C) No. 25420760.

Author Contributions: Y.S. and T.O. planned the present study, and wrote the manuscript. Y.S. prepared the samples, and collected the data. T.O. supervised the project.

Conflicts of Interest: The authors declare no conflict of interest.

References

1. Kumar, M.M.; Palkar, V.R.; Srinivas, K.; Suryanarayana, S.V. Ferroelectricity in a pure $BiFeO_3$ ceramic. *Appl. Phys. Lett.* **2000**, *76*, 2764–2766. [CrossRef]
2. Wang, J.; Neaton, J.B.; Zheng, H.; Nagarajan, V.; Ogale, S.B.; Liu, B.; Viehland, D.; Vaithyanathan, V.; Schlom, D.G.; Waghmare, U.V.; et al. Epitaxial $BiFeO_3$ multiferroic thin film heterostructures. *Science* **2003**, *299*, 1719–2722. [CrossRef] [PubMed]
3. Zhao, T.; Scholl, A.; Zavaliche, F.; Lee, K.; Barry, M.; Doran, A.; Cruz, M.P.; Chu, Y.H.; Ederer, C.; Spaldin, N.A.; et al. Electrical control of antiferromagnetic domains in multiferroic $BiFeO_3$ films at room temperature. *Nat. Mater.* **2006**, *5*, 823–829. [CrossRef] [PubMed]
4. Allibe, J.; Fusil, S.; Bouzehouane, F.; Daumont, C.; Sando, D.; Jacquet, E.; Deranlot, C.; Bibes, M.; Barthèlèmy, A. Room temperature electrical manipulation of giant magnetoresistance in spin valves exchange-biased with $BiFeO_3$. *Nano Lett.* **2012**, *12*, 1141–1145. [CrossRef] [PubMed]
5. Li, M.; Zhuge, F.; Zhu, X.; Yin, K.; Wang, J.; Liu, Y.; He, C.; Chen, B.; Li, R.-W. Nonvolatile resistive switching in metal/La-doped $BiFeO_3$/Pt sandwiches. *Nanotechnology* **2010**, *21*, 425202. [CrossRef] [PubMed]
6. Choi, T.; Lee, S.; Choi, Y.J.; Kiryukhin, V.; Cheong, S.-W. Switchable ferroelectric diode and photovoltaic effect in $BiFeO_3$. *Science* **2009**, *324*, 63–66. [CrossRef] [PubMed]
7. Sarkar, A.; Khan, G.G.; Chaudhuri, A.; Das, A.; Mandal, K. Multifunctional $BiFeO_3/TiO_2$ nano-heterostructure: Photo-ferroelectricity, rectifying transport, and nonvolatile resistive switching property. *Appl. Phys. Lett.* **2016**, *108*, 033112. [CrossRef]
8. Liu, Z.; Yang, F. Photovoltaic effect of $BiFeO_3$/poly(3-hexylthiophene) heterojunction. *Phys. Status Solidi RRL* **2011**, *5*, 367–369. [CrossRef]
9. Zhao, P.; Bian, L.; Wang, L.; Xu, J.; Chang, A. Enhanced open voltage of $BiFeO_3$ polycrystalline film by surface modification of organolead halide perovskite. *Appl. Phys. Lett.* **2014**, *105*, 013901. [CrossRef]
10. Yang, Y.; Xu, W.; Xu, X.; Wang, Y.; Yuan, G.; Wang, Y.; Liu, Z. The enhanced photocurrent of epitaxial $BiFeO_3$ film at 130 °C. *J. Appl. Phys.* **2016**, *119*, 044102. [CrossRef]
11. Chakrabartty, J.; Nechache, R.; Harnagea, C.; Li, S.; Rosei, F. Enhanced photovoltaic properties in bilayer $BiFeO_3$/Bi-Mn-O thin films. *Nanotechnology* **2016**, *27*, 215402. [CrossRef] [PubMed]
12. Kojima, A.; Teshima, K.; Shirai, Y.; Miyasaka, T. Organometal Halide perovskites as visible-light sensitizers for photovoltaic cells. *J. Am. Chem. Soc.* **2009**, *131*, 6050–6051. [CrossRef] [PubMed]
13. Im, J.-H.; Lee, C.-R.; Lee, J.-W.; Park, S.-W.; Park, N.-G. 6.5% efficient perovskite quantum-dot-sensitized solar cell. *Nanoscele* **2011**, *3*, 4088–4093. [CrossRef] [PubMed]
14. Kim, H.-S.; Lee, C.-R.; Im, J.-H.; Lee, K.-B.; Moehl, T.; Marchioro, A.; Moon, S.-J.; Humphry-Baker, R.; Yum, J.-H.; Moser, J.E.; et al. Lead iodide perovskite sensitized all-solid-state submicron thin film mesoscopic solar cell with efficiency exceeding 9%. *Sci. Rep.* **2012**, *2*, 591. [CrossRef] [PubMed]
15. Kim, H.-S.; Lee, L.-W.; Yantara, N.; Boix, P.P.; Kulkarni, S.A.; Mhaisalkar, S.; Grätzel, M.; Park, N.-G. High efficiency solid-state sensitized solar cell-based on submicrometer rutile TiO_2 nanorods and $CH_3NH_3PbI_3$ perovskite sensitizer. *Nano Lett.* **2013**, *13*, 2412–2417. [CrossRef] [PubMed]
16. Zhou, H.; Chen, Q.; Li, G.; Luo, S.; Song, T.-B.; Duan, H.-S.; Hong, Z.; You, J.; Liu, Y.; Yang, Y. Interface engineering of highly efficient perovskite solar cells. *Science* **2014**, *345*, 542–546. [CrossRef] [PubMed]
17. Jeon, N.J.; Noh, J.H.; Yang, W.S.; Kim, Y.C.; Ryu, S.; Seo, J.; Seok, S.I. Compositional engineering of perovskite materials for high-performance solar cells. *Nature* **2015**, *517*, 476–480. [CrossRef] [PubMed]
18. Bi, D.; Yi, C.; Luo, J.; Décoppet, J.-D.; Zhang, F.; Zakeeruddin, S.M.; Li, X.; Hagfeldt, A.; Grätzel, M. Polymer-templated nucleation and crystal growth of perovskite films for solar cells with efficiency greater than 21%. *Nat. Energy* **2016**, *1*, 16142. [CrossRef]
19. Chart of Best Research-Cell Efficiencies provided by National Renewable Energy Laboratory. Available online: http://www.nrel.gov/pv/assets/images/efficiency_chart.jpg (accessed on 2 December 2016).
20. Wang, Y.; Jiang, Q.-H.; He, H.-C.; Nan, C.-W. Multiferroic $BiFeO_3$ thin films prepared via a simple sol-gel method. *Appl. Phys. Lett.* **2006**, *88*, 142503. [CrossRef]
21. Wu, F.; Guo, Y.; Zhang, Y.; Duan, H.; Li, H.; Liu, H. Enhanced photovoltaic performance in polycrystalline $BiFeO_3$ thin film/ZnO nanorod heterojunctions. *J. Phys. Chem. C* **2014**, *118*, 15200–15206. [CrossRef]
22. Noh, J.H.; Im, S.H.; Heo, J.H.; Mandal, T.N.; Seok, S.I. Chemical management for colorful, efficient, and stable inorganic-organic hybrid nanostructured solar cells. *Nano Lett.* **2013**, *13*, 1764–1769. [CrossRef] [PubMed]

23. Shirahata, Y.; Suzuki, A.; Oku, T. Fabrication and characterization of bismuth ferrite as an electron transport layer in perovskite photovoltaic devices. *J. Ceram. Soc. Jpn.* **2016**, *124*, 602–605. [CrossRef]
24. Oku, T.; Zushi, M.; Imanishi, Y.; Suzuki, A.; Suzuki, K. Microstructures and photovoltaic properties of perovskite-type $CH_3NH_3PbI_3$ compounds. *Appl. Phys. Express* **2014**, *7*, 121601. [CrossRef]
25. Zushi, M.; Suzuki, A.; Akiyama, T.; Oku, T. Fabrication and characterization of $TiO_2/CH_3NH_3PbI_3$-based photovoltaic devices. *Chem. Lett.* **2014**, *43*, 916–918. [CrossRef]
26. Suzuki, A.; Okada, H.; Oku, T. Fabrication and characterization of $CH_3NH_3PbI_{3-x-y}Br_xCl_y$ perovskite solar cells. *Energies* **2016**, *9*, 346. [CrossRef]
27. Oku, T.; Suzuki, K.; Suzuki, A. Effects of chlorine addition to perovskite-type $CH_3NH_3PbI_3$ photovoltaic devices. *J. Ceram. Soc. Jpn.* **2016**, *124*, 234–238. [CrossRef]
28. Oku, T.; Ohishi, Y.; Suzuki, A. Effects of antimony addition to perovskite-type $CH_3NH_3PbI_3$ photovoltaic devices. *Chem. Lett.* **2016**, *45*, 134–136. [CrossRef]
29. Ohishi, Y.; Oku, T.; Suzuki, A. Fabrication and characterization of perovskite-based $CH_3NH_3Pb_{1\text{-}x}Ge_xI_3$, $CH_3NH_3Pb_{1\text{-}x}Tl_xI_3$ and $CH_3NH_3Pb_{1\text{-}x}In_xI_3$ photovoltaic devices. *AIP Conf. Proc.* **2016**, *1709*, 020020.
30. Shi, D.; Qin, X.; Li, Y.; He, Y.; Zhong, C.; Pan, J.; Dong, H.; Xu, W.; Li, T.; Hu, W.; Brédas, J.-L.; Bakr, O.M. Spiro-OMeTAD single crystals: Remarkably enhanced charge-carrier transport via mesoscale ordering. *Sci. Adv.* **2016**, *2*, e1501491. [CrossRef] [PubMed]
31. Kubel, H.; Schmid, H. Structure of a ferroelectric and ferroelastic monodomain crystal of the perovskite $BiFeO_3$. *Acta Cryst.* **1990**, *B46*, 698–702. [CrossRef]
32. Tang, X.; Dai, J.; Zhu, X.; Yin, L.; Ang, Y.; Song, W.; Yang, Z.; Sun, Y.; Zhang, R. Individual-layer thickness effects on the preferred *c*-axis-oriented $BiFeO_3$ films by chemical solution deposition. *J. Am. Ceram. Soc.* **2010**, *93*, 1682–1687.
33. Polomska, M.; Kaczmarek, W.; Pająk, Z. Electric and magnetic properties of $(Bi_{1-x}La_x)FeO_3$ solid solutions. *Phys. Stat. Solidi (a)* **1974**, *23*, 567–574. [CrossRef]
34. Gao, F.; Chen, X.; Yin, K.; Dong, S.; Ren, Z.; Yuan, F.; Yu, T.; Zou, Z.; Liu, J.-M. Visible-light photocatalytic properties of weak magnetic $BiFeO_3$ nanoparticles. *Adv. Mater.* **2007**, *19*, 2889–2892. [CrossRef]
35. Keskin, V.; Gupta, A.; Szulczewski, G. Solution processed $TiO_2/BiFeO_3$/poly(3-hexylthiophene) solar cells. *Mater. Lett.* **2015**, *159*, 305–308. [CrossRef]
36. Sun, Y.; Liu, Z.; Zeng, J.; Yan, J.; Shi, D.; Liu, H. Photovoltaic effects in polarized polycrystalline $BiFeO_3$ films. *J. Electron. Mater.* **2015**, *44*, 4207–4212. [CrossRef]
37. Xu, X.; Lin, Y.-H.; Li, P.; Shu, L.; Nan, C.-W. Synthesis and photocatalytic behaviors of high surface area $BiFeO_3$ thin films. *J. Am. Ceram. Soc.* **2011**, *94*, 2296–2299. [CrossRef]
38. Inorganic Material Database of National Institute for Materials Science. Available online: http://crystdb.nims.go.jp/index_en.html (accessed on 2 December 2016).
39. Sen, P.; Dey, A.; Mukhopadhyay, A.K.; Bandyopadhyay, S.K.; Himanshu, A.K. Nano indentation behaviour of nano $BiFeO_3$. *Ceram. Int.* **2012**, *38*, 1347–1352. [CrossRef]
40. Zhao, X.; Park, N.-G. Stability issues on perovskite solar cells. *Photonics* **2015**, *2*, 1139–1151. [CrossRef]
41. Scharber, M.C.; Mühlbacher, D.; Koppe, M.; Denk, P.; Waldauf, C.; Heeger, A.J.; Brabec, C. Design rules for donors in bulk-heterojunction solar cells—Towards 10 % energy-conversion efficiency. *Adv. Mater.* **2006**, *18*, 789–794. [CrossRef]
42. Kim, H.D.; Ohkita, H.; Benten, H.; Ito, S. Photovoltaic performance of Perovskite Solar Cells with Different Grain Sizes. *Adv. Mater.* **2016**, *28*, 917–922. [CrossRef] [PubMed]